PHYSICAL REVIEW E **100**, 042111 (2019)

Turing-like patterns in an asymmetric dynamic Ising model

Mélody Merle,[*] Laura Messio,[†] and Julien Mozziconacci[‡]
Sorbonne Université, CNRS, Laboratoire de Physique Théorique de la Matière Condensée, LPTMC, F-75005 Paris, France

(Received 26 March 2019; revised manuscript received 25 July 2019; published 8 October 2019)

To investigate novel aspects of pattern formation in spin systems, we use a mapping between reactive concentrations in a reaction-diffusion system and spin orientations in a dynamic multiple-spin Ising model. While pattern formation in Ising models always relies on infinite-range interactions, this mapping allows us to design a finite-range-interactions Ising model that can produce patterns observed in reaction-diffusion systems including Turing patterns with a tunable typical length scale. This model has asymmetric interactions and several spin types coexisting at a site. While we use the example of genetic regulation during embryogenesis to build our model, it can be used to study the behavior of other complex systems of interacting agents.

DOI: 10.1103/PhysRevE.100.042111

I. INTRODUCTION

The mechanisms underlying global pattern formation from local interactions are studied in many fields of physics, chemistry, and biology [1–3]. Reaction diffusion is possibly the most widespread patterning model. It uses continuous variables such as the concentrations of chemical species that can form complex patterns, e.g., stripes, propagating fronts, and oscillatory waves [4]. Another class of pattern formation models are Ising models. Ising variables are two-state (up and down) discrete spins interacting on a lattice. One can distinguish two types of interactions: infinite and finite range. Infinite-range interactions are more commonly referred to as long-range interactions, i.e., decreasing with the distance as a power law $1/r^{\alpha}$ with α larger than or equal to the spatial dimension. Infinite- and finite-range interactions show differences in terms of behavior and are investigated using specific computational methods [5]. In terms of patterning, finite-range interactions mostly lead to ferromagnetic (all spins up or down) or antiferromagnetic (alternating up and down spin) states. In the presence of frustration, one-site width stripes can also occur [6]. On the other hand, infinite-range interactions can lead to the formation of more complex patterns. The combination of ferromagnetic nearest-neighbor interactions with antiferromagnetic infinite-range interactions found, for instance, in ultrathin magnetic films [7,8] is known to produce patterns such as mazes or bubbles. Up to now, infinite-range interactions were considered a necessary condition for the formation of patterns with a typical width of several lattice constants. Our goal in the present paper is to derive a variant of the Ising model which produces such patterns without infinite-range interactions.

Reaction-diffusion and Ising models are both well adapted to describe emergent collective behaviors from individual evolution rules. Yet, they have been confronted in few restricted cases. An example is the rigorous proof of the existence of traveling fronts in a ferromagnetic Ising model under Glauber dynamics using a mapping of the magnetization evolution equation with the reaction-diffusion Allan-Cahn equation [9,10].

In this paper, we build upon the similarities between reaction-diffusion and Ising models to construct a dynamic finite-range Ising model giving rise to complex patterns. We introduce in Sec. III a stochastic reaction-diffusion automaton (SRDA) on a lattice, inspired by embryogenesis (Sec. II). Then we construct in Sec. IV our asymmetric dynamic Ising model (ADIM) and establish a mapping between the ADIM and the SRDA in Sec. V. From this mapping we show in Sec. VI that the ADIM can reproduce the variety of patterns observed in reaction-diffusion systems even if it only relies on finite-range interactions.

II. AN ASIDE ON EMBRYOGENESIS

One of the most emblematic example of pattern formation is embryogenesis, which motivated Turing to develop his well-known reaction-diffusion model in 1952 [4]. The major question in this field is to understand how initially identical cells can express different genes to form various tissues and organs at the proper time and location during the development of the embryo.

Turing proposed that interactions between diffusing gene products (called hereafter species) could lead to the spatial organization of gene expression. In the case of the so-called activator-inhibitor model, two species (an activator a and an inhibitor b) can self-organize in stripes, dots, or mazelike patterns. This is driven by three main ingredients: an autocatalysis of a, an asymmetry in reciprocal interactions (i.e., a enhances the formation of b while b penalizes the formation of a), and a quantitative difference in their diffusion coefficients. Besides these *self-organized* patterns [11–13] suggested by Turing, embryogenesis provides examples of *externally driven* patterns that are preformed at large scales, for instance, by chemical gradients in the case of *Drosophila*'s fertilized egg [14,15]. These gradients activate specific genes in different

---

[*] merle@lptmc.jussieu.fr
[†] messio@lptmc.jussieu.fr
[‡] mozziconacci@lptmc.jussieu.fr

locations of the embryo and the products of these genes subsequently act on other genes in a combinatorial manner. In the current view, the spatial regulation of gene expression in developing embryos is explained by combinations of these two different and complementary classes of scenarios [16].

Various models implementing these two classes have been proposed, either based on differential equations or on cellular automata [17]. Recently, an Ising model [18] has also been developed to model gene patterning during embryogenesis. Each spin represents a gene that can be in one of the two states: active or inactive. Each site represents a nucleus and can contain several spins (genes). The spatial proximity between nuclei defines the interaction lattice (nonzero couplings), while coupling values defines the interaction network between spins (genes). These couplings are a simplification of the molecular mechanisms at work: gene transcription in RNA, RNA translation in proteins, and protein diffusion to neighboring nuclei where they can modify the transcription rate of other genes. While being different from more detailed reaction-diffusion models, this Ising model features the most important ingredient: short-range interactions between spins (genes) [18]. Based on this similarity, we also placed ourselves in this context to build an extended variant of the Ising model, implementing asymmetric interactions between spin types, that could lead to Turing patterns. To achieve this goal, we start by constructing a reference reaction-diffusion model in the next section.

III. STOCHASTIC REACTION-DIFFUSION AUTOMATON

Reaction-diffusion models describe the evolution in time and space of the concentrations $\mathbf{c} = (c_a, c_b, \dots)$ of n_s chemical species $a, b, \dots$ undergoing two processes: diffusion, associated to diffusion coefficients $D_a, D_b, \dots,$ and local reactions $R_a(\mathbf{c}, g), R_b(\mathbf{c}, g), \dots,$ resulting in the creation of units of $a, b, \dots$ per time unit, where g is a possible external gradient forcing the system. The continuous space and time equations are for each species a of the form

$$\partial_t c_a = D_a \nabla^2 c_a + R_a(\mathbf{c}, g). \tag{1}$$

As a discrete space and time model of reaction diffusion, we use here a probabilistic automaton on a one-dimensional (1D) lattice. The vector $\mathbf{c}_i(t) = (c_{ia}(t), c_{ib}(t), \dots)$ contains the concentrations of the n_s considered species on each lattice site i at discrete time t. The external gradient g is a prescribed time-independent additional species of concentration g_i on site i. Each time step is divided into three substeps. The first one ($t \to t'$) is the production event: each concentration is incremented by 1 with probability

$$P_{ia}^{\text{prod}} = \frac{1}{1 + e^{-u_a(\mathbf{c}_i, g_i)}}. \tag{2}$$

It is a common usage to model gene regulation by sigmoidal functions. This exact form has been used for *Drosophila* development modeling [19]. We choose $u_a(\mathbf{c}_i, g_i)$ of the form

$$u_a(\mathbf{c}_i, g_i) = \sum_b (\phi_{ba} c_{ib}) + \kappa_a g_i - \theta_0, \tag{3}$$

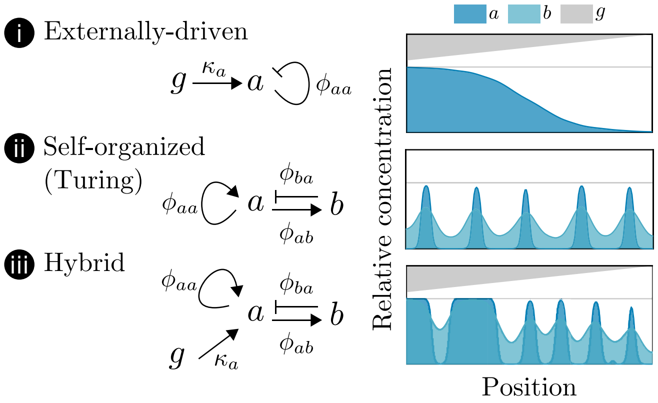

FIG. 1. The SRDA recapitulates different patterning mechanisms, illustrated here on a 1D lattice. (i) Externally driven pattern by a linear external gradient g. (ii) Self-organized pattern, here Turing stripes. (iii) Hybrid pattern which is a combination of both mechanisms. Corresponding interaction networks are shown with → and ⊣ symbols representing, respectively, activation and inhibition.

where the ϕ_{ba} are the reaction constants between species (the sum is over all species, including a itself), κ_a represents the effects of the gradient g on species a, and θ_0 is an activation threshold common to all species.

The second event ($t' \to t''$) is diffusion, approximated by a Gaussian kernel G_{σ_a} of standard deviation σ_a and mean value zero:

$$c_{ia}(t'') = \sum_{|j-i|<2\sigma_a} G_{\sigma_a}(|j - i|) c_{ja}(t'). \tag{4}$$

The third event ($t'' \to t + 1$) is degradation, assumed to occur at the same rate ε for all species:

$$c_{ia}(t + 1) = \varepsilon c_{ia}(t''), \tag{5}$$

where $0 < \varepsilon < 1$.

To represent the steady states, concentrations are normalized by $c_{\max} = \frac{\varepsilon}{1-\varepsilon}$, so $c^* = \frac{c}{c_{\max}}$ is comprised between 0 and 1. As described in Sec. II, two classes of patterns can emerge from our model: gradient-induced patterning [Fig. 1(i)] and Turing instabilities [Fig. 1(ii)]. The two types of mechanisms can be combined [Fig. 1(iii)], leading to the appearance of hybrid patterns [16].

IV. ASYMMETRIC DYNAMIC ISING MODEL

The classical Ising model was created in 1920 [20] as a toy model describing ferromagnetism. The spins are bivalued (usually $S_i = \pm 1$, but here, we equivalently choose $S_i = 0, 1$). They are placed on a lattice and interact with their nearest neighbors with an interaction constant $J > 0$ that tends to align them. In the presence of a space-dependent magnetic field h_i, the energy of the system is

$$E = -J \sum_i \sum_{j \in \partial_i} S_i S_j - \sum_i h_i S_i, \tag{6}$$

where ∂_i contains the nearest neighbors of site i.

The first step to map our reaction-diffusion automaton is to design a multiple-spin Ising model, similarly to that in [18].

To each site i of the lattice, we associate n_s spin types corresponding to the different species $a, b, \dots$. S_i becomes a vector $\mathbf{S}_\mathrm{i} = (s_{ia}, s_{ib}, \dots)$ of components 0 or 1. The concentration of the SRDA now corresponds to the average value of the spin, called the magnetization. Each spin type interacts with all other spin types including itself. We thus rewrite J as a matrix $\bar{J}$ whose coefficient J_{ab} represents the interactions between a spins and b spins. To mimic the gradient effect on the different genes, h_i is supposed to be coupled differently to each spin type and we introduce a coupling vector $\mathbf{K} = (k_a, k_b, \dots)$, where k_a represents the effect of h_i on the a spins. Equation (6) becomes

$$E = -\sum_i \sum_{j \in \partial_i} \mathbf{S}_\mathrm{j}{}^t \bar{J} \mathbf{S}_\mathrm{i} - \sum_i h_i \mathbf{K} \mathbf{S}_\mathrm{i}. \tag{7}$$

To get patterns typical of reaction diffusion, we also introduce a spin-type-dependent interaction range r_a. An a spin now acts on its neighboring sites up to a distance r_a, including itself. We denote by ∂_{ia} this set of spins (e.g., $\partial_{ia} = [i - r_a : i + r_a]$ on a 1D chain). The interaction parameters are rescaled using the volume $V_{\partial_{ia}}$, which is the number of sites in ∂_{ia} (e.g., $V_{\partial_{ia}} = 2r_a + 1$ in one dimension). We notice that only the average values $\frac{J_{ab}+J_{ba}}{2}$ are important in the determination of the equilibrium state of Eq. (7), obtained at finite temperature $T \neq 0$ using, e.g., the Metropolis algorithm [21]. However, the matrix $\bar{J}$ needs to be effectively asymmetric to reproduce the asymmetry of the reaction constants ϕ_{ab} leading to the formation of interesting patterns. We thus take a step further from [18] by implementing parallel dynamics in our model, similarly to kinetic asymmetric Ising models [22,23], making it a nonequilibrium model.

At each time step t, we calculate an effective field $h_{ia}^{\mathrm{eff}}(t)$ influencing the s_{ia} spin:

$$h_{ia}^{\mathrm{eff}}(t) = \sum_b \left(\frac{J_{ba}}{V_{\partial_{ib}}} \sum_{j \in \partial_{ib}} s_{jb}(t) \right) + k_a h_i - h_0, \tag{8}$$

where we introduce h_0, a homogeneous external gradient.

TABLE I. Correspondence between parameters of the models.

SRDA		ADIM	
Diffusion constant	σ	r	Interaction range
Reaction constant	$\bar{\phi}$	$\bar{J}$	Interaction strength
Reaction constant with gradient	κ	k	Coupling with linear field
Activation threshold	θ_0	h_0	Homogeneous external field
Degradation	$\varepsilon = 0.5$		
Noise		$T = 1$	Temperature

All spins are then updated to give the configuration at time $t + 1$ according to the following probability distribution:

$$P(s_{ia}(t+1)) = \frac{e^{-\beta h_{ia}^{\mathrm{eff}}(t) s_{ia}(t+1)}}{2\cosh\left(\beta h_{ia}^{\mathrm{eff}}(t)\right)}, \tag{9}$$

where $\beta = 1/T$. The temperature T accounts for the noisiness of the system.

V. MODEL COMPARISON

The SRDA and ADIM are both governed by Markovian dynamics and share important features: asymmetry of the coupling matrices and locality of the interactions (see Appendix A for the detailed numerical implementation). In the ADIM, however, local reactions and transport are merged in nearest-neighbor interactions. Still, many parameters appear to have similar roles: $\bar{J}$ and Φ, k and κ, h_0 and θ_0, and r and σ, as presented in Table I. Two parameters are nevertheless model specific: the degradation rate ε and the temperature T.

We wish to investigate the similarity in patterns that can be obtained by confronting the two models. We study the case $n_s = 1$, which corresponds to a classical Ising model under a space-dependent external field. We fix $T = 1$ in the ADIM since this temperature gives the most direct equivalence with Eq. (2) (see Appendix B). For the sake of simplicity, we fix $r_a = \sigma_a = 1$ so that the only interaction is between nearest neighbors and we choose the space-dependent external field to be linear. In this condition, we show by a calculation using

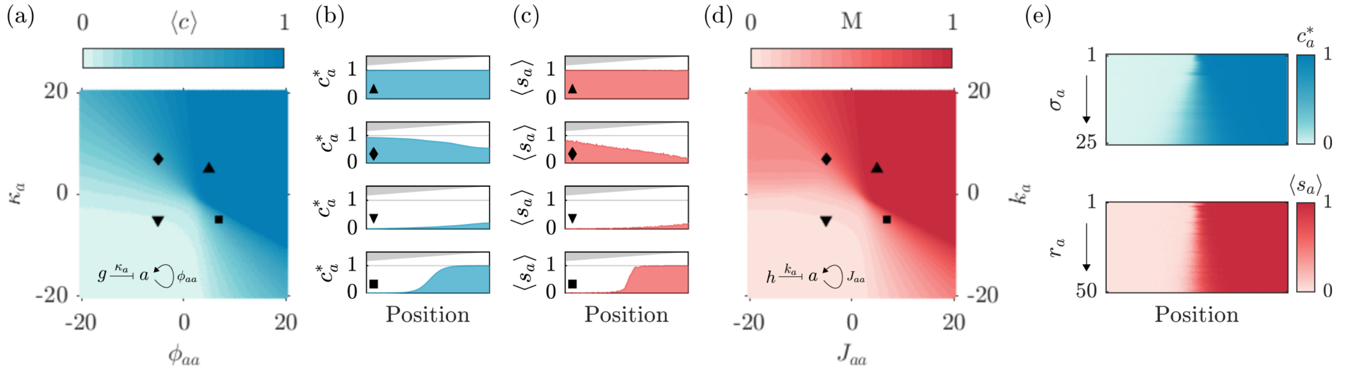

FIG. 2. Comparison of models for $n_s = 1$, i.e., interaction networks as represented in insets in (a) and (d) with two parameters: self-regulation ϕ_{aa}/J_{aa} and external gradient effect κ_a/k_a. Other parameters are fixed: $\theta_0 = h_0 = 1$, $\sigma_a = r_a = 1$, $\varepsilon = 0.5$, and $T = 1$. (a) Mean concentration $\langle c \rangle$ and (d) magnetization M in the parameter space (ϕ_{aa}, κ_a) for the SRDA and (J_{aa}, k_a) for the ADIM. (b, c) Spatial patterns obtained in both models for four sets of parameters representing the possible types of patterns (▲, fully activated; ◆, gradientlike; ▼, fully inhibited; ■, sharp boundary). (d) Spatial parameters (diffusion coefficient σ_a and interaction range r_a) effect on the sharpness of the ■ pattern.

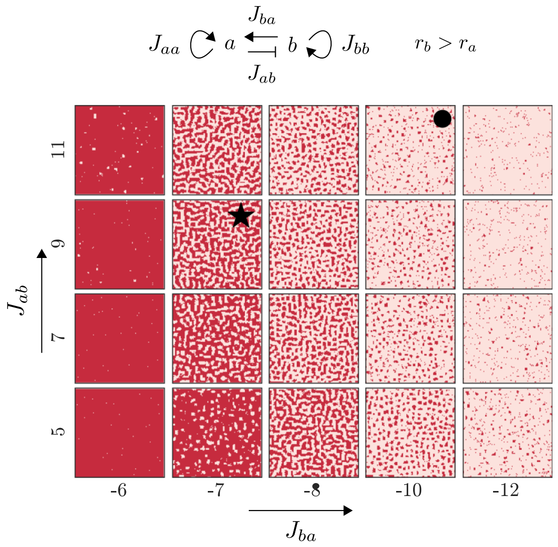

FIG. 3. 2D ADIM simulations on a 128 × 128 periodic square lattice with $h_0 = 1$, $r_a = 1$, $r_b = 5$, $J_{aa} = 13$, $J_{bb} = 0$, J_{ab} and J_{ba} varying, and $T = 1$. Dark red (dark gray) corresponds to $s_a = 1$ and pink (light gray) to $s_a = 0$. A variety of Turing-like patterns is observed including "maze" (★) and "bubbles" (●).

the homogeneous solutions in mean-field approximation (see Appendix B) that the degradation rate that gives the best mapping between interaction parameters in both models is $\varepsilon_{\text{opt}} = 0.5$.

Figures 2(a)–2(d) present the mean concentration $\langle c^* \rangle$ and the magnetization M of the patterns obtained by the SRDA and ADIM in the planes (ϕ_{aa}, κ_a) and (J_{aa}, k_a) with $h_0 = \theta_0 = 1$. They represent the fraction of time during which a is being produced or spins s_a are up, averaged over each positions. For all probed regions of the parameter space, very similar patterns are observed for both the ADIM and the SRDA. Two broad zones of $\langle c^* \rangle = M = 1$ and $\langle c^* \rangle = M = 0$ correspond to full activation (Fig, 2, ▲) and full inhibition (Fig. 2, ▼). The transition between theses two states can be done either through the formation and displacement of a sharp boundary (Fig. 2, ■), corresponding to strong inhibition by the external gradient and autoactivation, or by the appearance and intensification of a smooth gradientlike pattern (Fig. 2, ♦), corresponding to a gradient activation balanced by a null or very low autoinhibition.

Yet, the sharpness of the ■ pattern is different in both models. Intuitively this sharpness depends on the correlation length of the system. The difference in patterns thus reflects a quantitative difference between the roles of the diffusion coefficient and the interaction range. Figure 2(e) represents the evolution of the ■ pattern in SRDA and ADIM as a function of respectively σ_a and r_a. The maps confirm that σ_a and r_a are the spatial parameters that control the boundary sharpness. In both models, increasing these parameters causes an increase in the correlation lengths and thus a decrease of the border sharpness. It is therefore possible to choose a value for r_a for which the slope exactly matches the slope obtained for any given value of σ_a (see Appendix C for more discussion on this matter).

VI. TURING PATTERNS IN THE ADIM

In light of these similarities between SRDA and ADIM in the case $n_s = 1$, we now look at the case $n_s = 2$ with no external gradient and try to reproduce Turing patterns. To investigate a richer variety of Turing patterns, we also switch to a two-dimensional (2D) case with periodic boundary conditions. A main feature enabling Turing instabilities in reaction-diffusion models is the difference of diffusion coefficients for both species. Likewise, the ratio r_b/r_a, where a is the activator spin type and b is the inhibitor spin type, needs to be large enough to form patterns of different spin orientations. 2D patterns as a function of the interactions $J_{ab} > 0$ and $J_{ba} < 0$ are presented in Fig. 3(a) for $r_a = 1$ and $r_b = 5$, on a 128 × 128 square lattice. A subtle trade-off between the values of the interactions gives rise to different types of patterns, including "maze" (★) and "bubbles" (●). These two patterns are used for further analysis in the next part.

To quantitatively study the 2D patterns obtained with our ADIM, we compute the discrete 2D Fourier transform (FT) of s_a on our periodic square lattice of linear size n:

$$\tilde{s}_a(q_x, q_y) = \sum_{x=0}^{n-1} \sum_{y=0}^{n-1} e^{-\frac{2i\pi}{n}(xq_x + yq_y)} s_a(x, y). \tag{10}$$

These patterns have one characteristic length resulting in a circular distribution in the reciprocal space [Fig. 4(a),(c)-ii]. The FT gives two quantities: the pseudo-order parameter Λ and the characteristic length L_Λ. We average $\tilde{s}_a$ over circles of radius q to get the mean intensity $\lambda(q)$ and define the order parameter $\Lambda = \lambda(q_{\text{peak}})$ as the peak value of these curves. The corresponding characteristic length in the direct space is $L_\Lambda = \frac{1}{q_{\text{peak}}}$. For illustration, Fig. 4 shows the $\lambda(q)$ curves at different temperatures for both maze and bubbles patterns from Fig 2.

We first investigate the role of r_b in the emergence of patterns for a fixed $r_a = 1$. Figure 5(a) shows the maze pattern and its FT for different values of r_b. While there is no pattern for small values of r_b, maze patterns appear for higher values. Computing L_Λ/r_a for r_b ranging from 1 to 25 we conclude that the maze pattern appears for $r_b \geqslant 3$ [Fig. 5(b)]. The characteristic length of the pattern increases linearly with r_b with a coefficient close to 1. For higher values of r_a, L_Λ/r_a increases linearly with the ratio r_b/r_a with the same coefficient. We conclude that if one takes r_a as a unit length, the behavior of adimensional quantities L_Λ/r_a and r_b/r_a is independent of the lattice spacing. When the lattice spacing becomes small compared to the characteristic length r_a we can refine the value of the ratio r_b/r_a for which patterns appear. In this case we find that this value tends towards 2.

We next investigate the effect of temperature on the stability of these patterns using the pseudo-order parameter Λ defined above. In infinite-range interacting Ising models at equilibrium, phase transitions between smectic, nematic, or liquid phases can occur when T varies [24]. Here, the various patterns do not break any symmetry and no such phase transition can occur. Figure 6 shows Λ for different system sizes and different temperatures. A dynamic crossover occurs between a patterned and a disordered phase for both patterns,

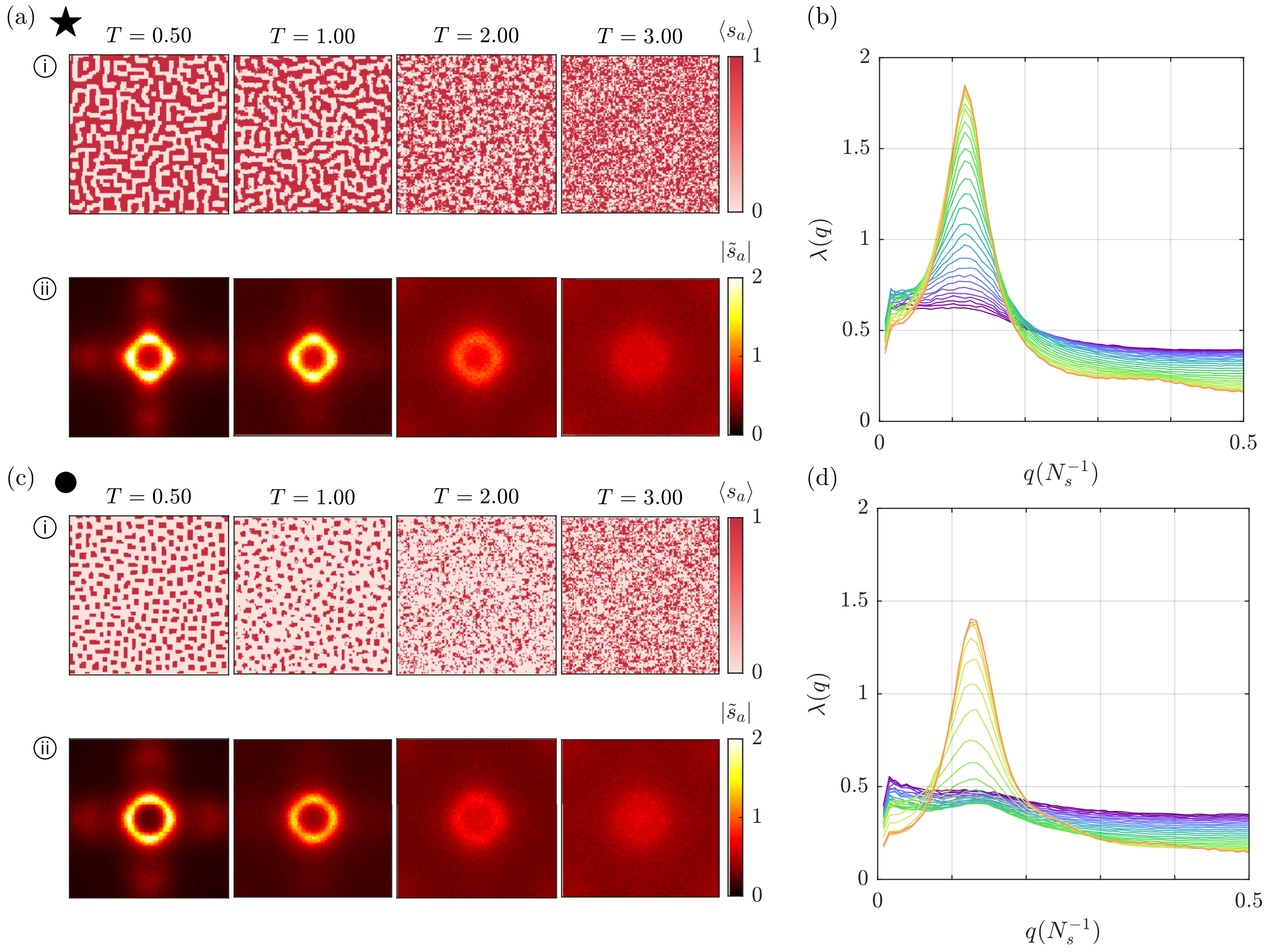

FIG. 4. (a, c) (i) Snapshots of patterns in 128 × 128 periodic square boxes for $T = 0.5, 1, 2, 3$ for respectively maze and bubbles patterns introduced in main text [dark red (dark gray) corresponds to $s_a = 1$ and pink (light gray) to $s_a = 0$] and (ii) 2D Fourier transforms of these patterns averaged on $n = 100$ independent simulations. (b, d) Mean value $\lambda(q)$ of the FT over circles of radius q over different temperatures between 0 and 3. The peak value of this distribution gives us the order parameter Λ. The corresponding length in direct space L_Λ is the characteristic length of the pattern.

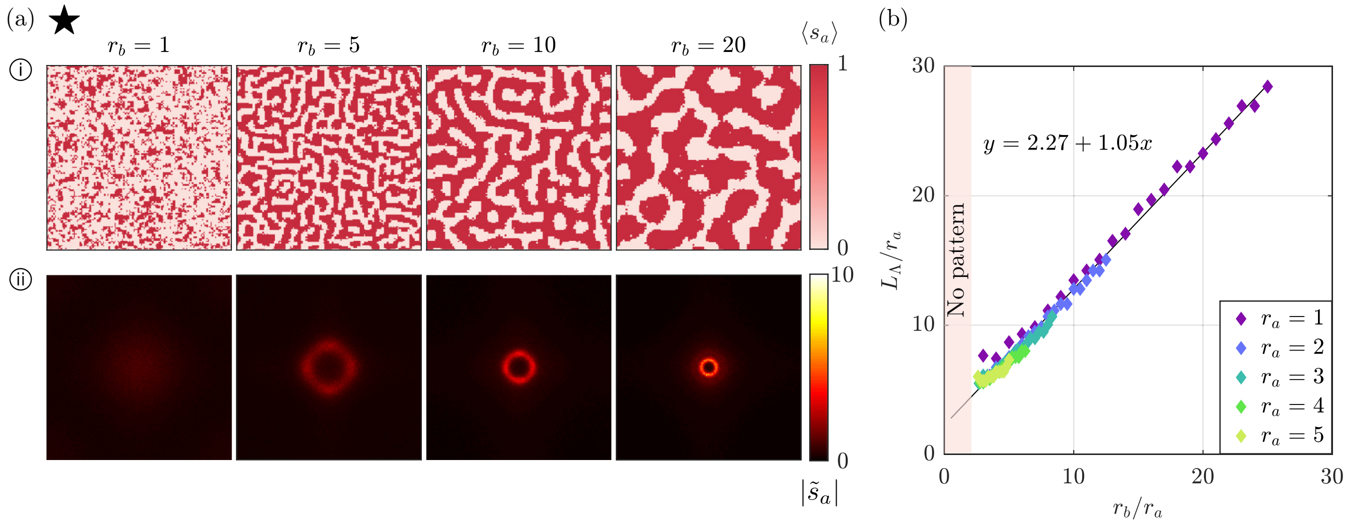

FIG. 5. (a) (i) 128 × 128 zoomed snapshots of the maze pattern obtained in simulations on 512 × 512 periodic square lattices with $r_a = 1$ and $r_b = 1, 5, 10, 20$. Dark red (dark gray) corresponds to $s_a = 1$ and pink (light gray) to $s_a = 0$. (ii) The corresponding 2D Fourier transforms averaged over $n = 20$ independent simulations. (b) The value of the typical length L_Λ / r_a of the patterns as a function of the ratio r_b / r_a for different values of r_a.

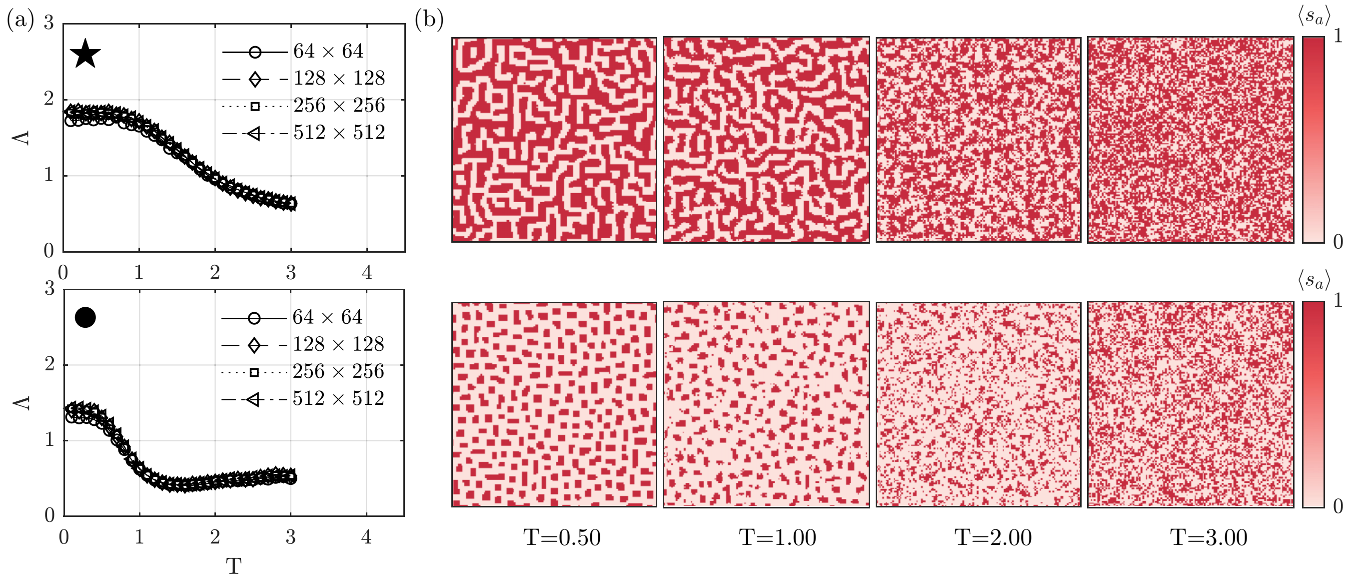

FIG. 6. (a) Pseudo-order parameter Λ as a function of temperature for maze (★) and bubbles (●) patterns issued from Fig. 3, obtained by averaging the FT over $n = 100$ independent simulations. $\Lambda = f(T)$ is computed for different system sizes. (b) 128×128 snapshots at different temperatures of the corresponding patterns. Dark red (dark gray) corresponds to $s_a = 1$ and pink (light gray) to $s_a = 0$.

albeit at different temperatures. The crossovers do not depend on the lattice size, thus excluding potential finite size effects.

In the Ising model, the temperature reflects thermal noise, whereas in a reaction-diffusion system, noise is related to the number of molecules: a lower number leads to larger relative fluctuations in the local concentrations. Molecular dynamics studies point out the importance of fluctuations for the emergence of Turing patterns [25]. Our results on the stability of patterns with temperature suggest on the other hand that if the number of molecules becomes too small (corresponding to high temperatures, and hence high fluctuations) the patterns could disappear.

VII. CONCLUSION

To summarize, using an embryogenesis-inspired mapping between an Ising model and a reaction-diffusion automaton, we have constructed the ADIM, a finite-range out-of-equilibrium Ising model that can give rise to Turing patterns with a typical length scale of several lattice spacings. Such Turing patterns had previously only been observed in infinite-range Ising models. It is worth noticing that our variant of the Ising model can be seen as a cellular automaton featuring rules similar to the ones which can be derived from reaction-diffusion equations (see for instance [26]). Our approach shows that a discrete toy model with different ranges of interaction and an asymmetry in the interaction coupling between species is sufficient to produce Turing-like patterns.

APPENDIX A: NUMERICAL METHODS

ADIM. The system is composed of N_S sites. On each site is associated n_s spin types. Parallel dynamics is implemented as follows.

We initialize the system at $t = 0$ by randomly attributing a value 0 or 1 at each of the $n_s \times N_S$ spins. At each time step t we calculate the effective field $h_{ia}^{\mathrm{eff}}(t)$ for each a-type spin on each site i:

$$h_{ia}^{\mathrm{eff}}(t) = \sum_b \left(\frac{J_{ba}}{V_{\partial_{ib}}} \sum_{j\in\partial_{ib}} s_{jb}(t) \right) + k_a h_i - h_0, \qquad \text{(A1)}$$

where J_{ba} is the action of b spins on a spins, h_i the value of the space-dependent external magnetic field at site i, k_a the coupling between $\mathbf{h}$ and a-type spins, and h_0 a global external field. ∂_{ib} designates the nearest neighbors of spin s_{ib}, defined by the interaction range r_b for b-spin type such as $\partial_{ib} = \{j, |j - i| < r_b\}$ and $V_{\partial ib} = \mathrm{Card}(\partial_{ib})$.

We calculate the corresponding Boltzmann probabilities:

$$P(s_{ia}(t+1) = 1) = \frac{e^{\beta h_{ia}^{\mathrm{eff}}(t)}}{2\cosh\left(\beta h_{ia}^{\mathrm{eff}}(t)\right)}, \qquad \text{(A2)}$$

where $\beta = T^{-1}$ is the inverse temperature.

In one dimensions, the simulation runs at a fixed temperature T. In two dimensions, the stationary state is calculated using a simulated annealing (SA) to avoid freezing in configurations with long relaxation times. The cooling strategy is exponential:

$$T_{SA}(t) = T_0 \times a^t \qquad \text{(A3)}$$

with $0 < a < 1$.

The spins at time $t + 1$ are simultaneously chosen according to these probabilities. The operation is repeated during n_t time steps, and in case of SA, a is chosen so that $T_{SA}(n_t) = T$, i.e., $a = (\frac{T}{T_0})^{n_t^{-1}}$. Then the simulation is pursued and recorded for n_{rec} time steps. Finally $\langle s_{ia}\rangle$ is obtained by averaging over the n_{rec} recorded configurations. Typically, $n_t = 250$ and $n_{\mathrm{rec}} = 50$.

SRDA. The system is composed of N_S sites at which is associated n_s species concentrations c_a. Each concentration is randomly chosen at $t = 0$ between 0 and 1. Each time step is subdivided into three events as presented in the main text. This is repeated for n_t time steps to reach the stationary state. Then each concentration is normalized by $c_{\max}$ to obtain $0 < c^*_{ia} < 1$. Typically, $n_t = 200$.

In both models, the boundary conditions are set to reflecting in the 1D case to have gradient-dependent patterns. In the 2D ADIM, we choose periodic boundary conditions.

APPENDIX B: DETERMINATION OF ε_{opt} USING HOMOGENEOUS STATIONARY SOLUTIONS

We use here the homogeneous steady-state solutions in mean-field approximation for both models to establish a relationship between parameters in the case of one species a ($n_s = 1$), and more specifically to find the optimal value ε_{opt} for which both models lead to the same patterns for equal network parameters.

ADIM. The mean-field approximation for the ADIM is [see Eq. (9)]

$$\langle s_{ia}\rangle = \frac{1}{1 + e^{\beta\langle h^{\text{eff}}_{ia}\rangle}}. \tag{B1}$$

For only one spin type a ($n_s = 1$),

$$\langle s_{ia}\rangle = \frac{1}{1 + e^{\beta\left[\frac{J_{aa}}{V_{\partial_{ia}}}\sum_{j\in\partial_{ia}}\langle s_{ja}\rangle + k_a h_i - h_0\right]}}. \tag{B2}$$

Since we consider a homogeneous state and we are in one dimension, $\sum_{j\in\partial_{ia}}\langle s_{ja}\rangle = (2r_a + 1)\langle s_{ia}\rangle$ and $V_{\partial_{ia}} = 2r_a + 1$, leading to

$$\langle s_{ia}\rangle = \frac{1}{1 + e^{\beta[J_{aa}\langle s_{ia}\rangle + k_a h_i - h_0]}}. \tag{B3}$$

SRDA. In the mean-field approximation for the SRDA model, we average over several realizations of time evolution for each time step. Thus, we replace the probabilistic increment of the production step [Eq. (2)] by a deterministic one:

$$c_{ia}(t') = c_{ia}(t) + \frac{1}{1 + e^{-u_a(\mathbf{c}_i, g_i)}}. \tag{B4}$$

By combining this new equation to the two other events, diffusion [Eq. (4)] and degradation [Eq. (5)], we get

$$c_{ia}(t+1) = \varepsilon\left[\sum_{|j-i|<2\sigma_a} G_{\sigma_a}(|j-i|)\left[c_{ja}(t) + \frac{1}{1 + e^{-u_a(\mathbf{c}_j)}}\right]\right]. \tag{B5}$$

in the classical approach of reaction-diffusion using partial differential equations, such as in Eq. (1), searching for a homogeneous steady state equates to looking for the solution of $R_a(\mathbf{c}, g) = 0$ since $\partial_t c_a = 0$ (steady state) and $\nabla^2 c_a = 0$ (homogeneous). In our SRDA, the homogeneity translates in $\forall j\ c_{ja}(t) = c_{ia}(t)$, and using the fact that $\sum_{r<2\sigma} G_\sigma(r) = 1$, we obtain

$$\sum_{|j-i|<2\sigma_a} G_{\sigma_a}(|j-i|)\left[c_{ja}(t) + \frac{1}{1 + e^{-u_a(\mathbf{c}_j)}}\right] = c_{ia}(t'), \tag{B6}$$

which leads to a simplification of Eq. (B5):

$$c_{ia}(t+1) = \varepsilon\left[c_{ia}(t) + \frac{1}{1 + e^{-u_a(\mathbf{c}_i, g_i)}}\right]. \tag{B7}$$

Being at steady state $c_{ia}(t+1) = c_{ia}(t)$, and using $c_{\max} = \frac{\varepsilon}{1-\varepsilon}$, we retrieve c^*:

$$c^*_{ia} = \frac{1}{1 + e^{-u_a(\mathbf{C}_i)}}. \tag{B8}$$

For $n_s = 1$,

$$c^*_{ia} = \frac{1}{1 + e^{\left[\phi_{aa}\frac{c^*_{ia}(1-\varepsilon)}{\varepsilon} + \kappa_a g_i - \theta_0\right]}}. \tag{B9}$$

Optimal mapping value of ε. Equations (B9) and (B1) are combined to search for the solution of $\langle s_{ia}\rangle = c^*_{ia}$, leading to

$$\beta[J_{aa}\langle s_{ja}\rangle + k_a h_i - h_0] = \frac{\phi_{aa}\varepsilon}{1-\varepsilon}c^*_{ia} + \kappa_a g_i - \theta_0. \tag{B10}$$

For $\beta = T^{-1} = 1$, identical network parameters ($J_{aa} = \phi_{aa}$, $k_a = \kappa_a$, and $h_0 = \theta_0$), and under the same external gradient ($h_i = g_i$), we get

$$\langle s_{ia}\rangle = \frac{\varepsilon}{1-\varepsilon}c^*_{ia}. \tag{B11}$$

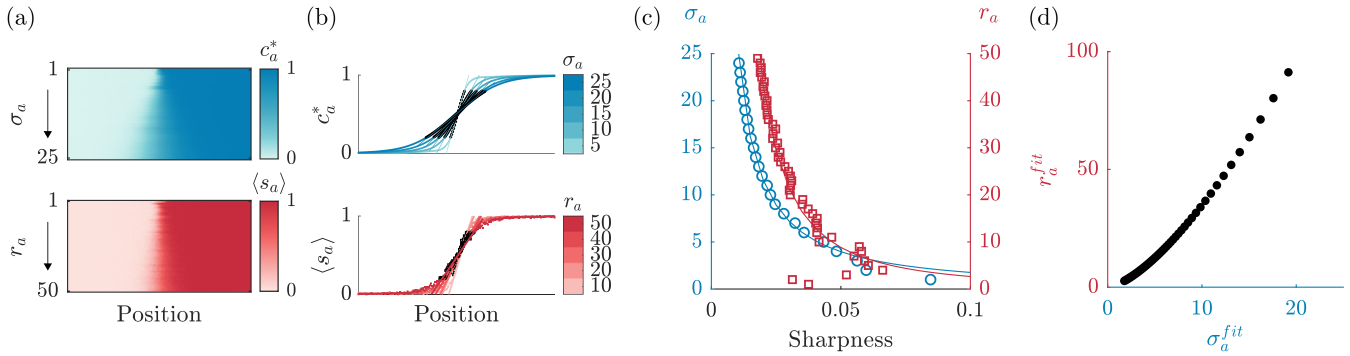

FIG. 7. Correspondence between r_a using the sharp-boundary pattern introduced in the main text (see Fig. 2). (a) Increasing the spatial parameters σ_a and r_a decreases the boundary sharpness. (b) Quantitative evaluation of the sharpness by fitting the boundary interface by an affine function. (c) σ_a (blue circle) and r_a (red square) as a function of the measured sharpness are fitted by power laws $y = \frac{a}{x^b}$. For any given sharpness, σ^{fit}_a and r^{fit}_a can be calculated using these fits. (d) r^{fit}_a as a function of σ^{fit}_a.

Finally, we obtain the optimal degradation parameter ε for which both models give an equivalent homogeneous steady state for equivalent parameters, as presented in the results of the main content of this paper (Fig. 2):

$$\varepsilon = 0.5. \tag{B12}$$

APPENDIX C: EQUIVALENCE BETWEEN σ_a AND r_a

To evaluate the correspondence between σ_a in the SRDA and r_a in the ADIM we use the sharp boundary pattern presented in the main text for $n_s = 1$ under a linear external gradient. This pattern appears when the spin or gene activates itself but is repressed by the gradient ($J_{aa} = 7$ and $k_a = -5$). As seen in the main text and shown again in Fig. 7(a), as σ_a or r_a increases, the sharpness of the boundary decreases. We first measure this sharpness by fitting the boundary interface ($0.2 < c_a^*, \langle s_a \rangle < 0.8$) by an affine function of the position [Fig. 7(b)]. The slope defines the sharpness of the boundary. Both the diffusion constant σ_a and the interaction range r_a as a function of sharpness are fitted by power laws $y = \frac{a}{x^b}$ [Fig. 7(c)]. From these fits we calculated σ_a^{fit} and r_a^{fit} for any given sharpness and plotting r_a^{fit} as a function of σ_a^{fit} gives us an equivalence between r_a and σ_a [Fig. 7(d)].

---

[1] V. Castets, E. Dulos, J. Boissonade, and P. De Kepper, Phys. Rev. Lett. **64**, 2953 (1990).

[2] A. Koch and H. Meinhardt, Rev. Mod. Phys. **66**, 1481 (1994).

[3] X. Diego, L. Marcon, P. Müller, and J. Sharpe, Phys. Rev. X **8**, 021071 (2018).

[4] A. M. Turing, Philos. Trans. R. Soc. London B **52**, 153 (1952).

[5] M. C. Angelini, G. Parisi, and F. Ricci-Tersenghi, Phys. Rev. E **89**, 062120 (2014).

[6] S. Jin, A. Sen, W. Guo, and A. W. Sandvik, Phys. Rev. B **87**, 144406 (2013).

[7] J. S. M. Fonseca, L. G. Rizzi, and N. A. Alves, Phys. Rev. E **86**, 011103 (2012).

[8] K. De'Bell, A. B. MacIsaac, and J. P. Whitehead, Rev. Mod. Phys. **72**, 225 (2000).

[9] A. De Masi, E. Orlandi, E. Presutti, and L. Triolo, Nonlinearity **7**, 633 (1994).

[10] A. De Masi, T. Gobron, and E. Presutti, Arch. Ration. Mech. Anal. **132**, 143 (1995).

[11] J. Cooke and E. C. Zeeman, J. Theor. Biol. **58**, 455 (1976).

[12] F. Corson, L. Couturier, H. Rouault, K. Mazouni, and F. Schweisguth, Science **356**, eaai7407 (2017).

[13] J. Cotterell, A. Robert-Moreno, and J. Sharpe, Cell Syst. **1**, 257 (2015).

[14] L. Wolpert, J. Theor. Biol. **25**, 1 (1969).

[15] T. Gregor, E. F. Wieschaus, A. P. McGregor, W. Bialek, and D. W. Tank, Cell **130**, 141 (2007).

[16] J. B. A. Green and J. Sharpe, Development (Cambridge, UK) **142**, 1203 (2015).

[17] J. Sharpe, Development (Cambridge, UK) **144**, 4214 (2017).

[18] P. Hillenbrand, U. Gerland, and G. Tkačik, PLoS ONE **11**, e0163628 (2016).

[19] G. R. Ilsley, J. Fisher, R. Apweiler, A. H. De Pace, and N. M. Luscombe, eLife **2**, e00522 (2013).

[20] S. G. Brush, Rev. Mod. Phys. **39**, 883 (1967).

[21] N. Metropolis and S. Ulam, J. Am. Stat. Assoc. **44**, 335 (1949).

[22] M. Mézard and J. Sakellariou, J. Stat. Mech. Theor. Exp. (2011) L07001.

[23] Y. Roudi and J. Hertz, Phys. Rev. Lett. **106**, 048702 (2011).

[24] A. Abanov, V. Kalatsky, V. L. Pokrovsky, and W. M. Saslow, Phys. Rev. B **51**, 1023 (1995).

[25] A. Lemarchand and B. Nowakowski, Europhys. Lett. **94**, 48004 (2011).

[26] J. R. Weimar and J.-P. Boon, Phys. Rev. E **49**, 1749 (1994).